

## Article

# Developing a CeS<sub>2</sub>/ZnS Quantum Dot Composite Nanomaterial as a High-Performance Cathode Material for Supercapacitor

Shan-Diao Xu, Li-Cheng Wu, Muhammad Adil , Lin-Feng Sheng, Zi-Yue Zhao, Kui Xu and Xin Chen \* 

Key Laboratory for Ultrafine Materials of Ministry of Education, and Shanghai Key Laboratory of Advanced Polymeric Materials, School of Materials Science and Engineering, East China University of Science and Technology, Shanghai 200237, China; y82220267@mail.ecust.edu.cn (S.-D.X.); y82230323@mail.ecust.edu.cn (L.-C.W.); y10230223@mail.ecust.edu.cn (M.A.);

y30240901@mail.ecust.edu.cn (L.-F.S.); y82230279@mail.ecust.edu.cn (Z.-Y.Z.); y82240239@mail.ecust.edu.cn (K.X.)

\* Correspondence: xinchen73@ecust.edu.cn

## Abstract

To develop high-performance electrode materials for supercapacitors, in this paper, a heterostructured composite material of cerium sulfide and zinc sulfide quantum dots (CeS<sub>2</sub>/ZnS QD) was successfully prepared by hydrothermal method. Characterization through scanning electron microscopy (SEM), X-ray diffraction (XRD), and transmission electron microscopy (TEM) showed that ZnS QD nanoparticles were uniformly composited with CeS<sub>2</sub>, effectively increasing the active sites surface area and shortening the ion diffusion path. Electrochemical tests show that the specific capacitance of this composite material reaches 2054 F/g at a current density of 1 A/g (specific capacity of about 256 mAh/g), significantly outperforming the specific capacitance of pure CeS<sub>2</sub> 787 F/g at 1 A/g (specific capacity 98 mAh/g). The asymmetric supercapacitor (ASC) assembled with CeS<sub>2</sub>/ZnS QD and activated carbon (AC) retained 84% capacitance after 10,000 charge–discharge cycles. Benefited from the synergistic effect between CeS<sub>2</sub> and ZnS QDs, the significantly improved electrochemical performance of the composite material suggests a promising strategy for designing rare-earth and QD-based advanced energy storage materials.



Academic Editor: Douglas Ivey

Received: 4 June 2025

Revised: 24 July 2025

Accepted: 28 July 2025

Published: 1 August 2025

**Citation:** Xu, S.-D.; Wu, L.-C.; Adil, M.; Sheng, L.-F.; Zhao, Z.-Y.; Xu, K.; Chen, X. Developing a CeS<sub>2</sub>/ZnS Quantum Dot Composite Nanomaterial as a High-Performance Cathode Material for Supercapacitor. *Batteries* **2025**, *11*, 289. <https://doi.org/10.3390/batteries11080289>

**Copyright:** © 2025 by the authors. Licensee MDPI, Basel, Switzerland. This article is an open access article distributed under the terms and conditions of the Creative Commons Attribution (CC BY) license (<https://creativecommons.org/licenses/by/4.0/>).

## 1. Introduction

As the world rapidly transitions from fossil fuels like natural gas, coal, and petroleum products to renewable energy sources like wind and solar power, the demand for energy storage devices is on the rise [1,2]. To alleviate these challenges, the emergence of renewable/green energy has become pivotal. Progression towards green energy helps reduce the carbon footprint, create job opportunities, lower energy dependence and help in conserving natural resources for years to come. Supercapacitors have attracted significant attention owing to their superior characteristics compared to conventional batteries. These advantages include rapid charge and discharge capabilities, extended cycle life, and high power density, making them particularly suitable for applications requiring quick outbursts of energy and frequent cycling [3]. In addition, supercapacitors exhibit an extended cycle life, capable of enduring up to millions of charge–discharge cycles with minimum performance deterioration. Supercapacitors possess a high power density, allowing them to deliver substantial power within a brief time interval [4–6]. At present, researchers are focused on developing advanced electrode materials with enhanced electrochemical performance [7].

Early research focused extensively on carbon-based materials (e.g., activated carbon, graphene) and conductive polymers (e.g., polyaniline, polypyrrole) due to their tunable porosity, high surface area, and cost-effectiveness [4,7–9]. However, these materials often suffer from limited energy density and mechanical instability during cycling. To overcome these limitations, transition metal sulfides (TMSs) have emerged as novel promising candidates owing to their rich redox chemistry, high theoretical capacitance, and structural diversity [10–12]. For instance, NiS and CoS<sub>2</sub> exhibit exceptional pseudocapacitive behavior but face challenges like poor conductivity and aggregation [13]. Cerium sulfide (CeS<sub>2</sub>), a rare-earth chalcogenide, has recently gained attention due to its high theoretical capacity, abundant oxidation states (Ce<sup>3+</sup>/Ce<sup>4+</sup>), and eco-friendliness ion [10,11]. Despite these advantages, pure CeS<sub>2</sub> suffers from sluggish ion kinetics and volume expansion during charge–discharge processes. Quantum dots (QDs), offer a potential solution due to their large surface area, quantum confinement effects, and tunable electronic properties [12,13]. Quantum dots (QDs), particularly ZnS QDs, provide a compelling solution due to their quantum confinement effects, high surface-to-volume ratio, and ability to facilitate electron transport [14,15]. Compared to carbonaceous or polymeric additives, ZnS QDs uniquely combine thermal/chemical stability with tunable bandgaps, enabling synergistic effects with CeS<sub>2</sub> to mitigate aggregation and shorten ion diffusion paths [16,17]. Srikant Sahoo et al. [18] successfully synthesized hierarchical flower-like nickel sulfide nanostructures and their composites with carbon quantum dots (NiS/CQD) via a facile hydrothermal method. The NiS/CQD composite demonstrated superior electrochemical energy storage performance as a supercapacitor electrode material, exhibiting a specific capacitance of 880 F/g at a current density of 2 A/g. Remarkably, the material maintained excellent cycling stability with negligible capacitance decay over 2000 charge–discharge cycles. The carbon quantum dots were derived from natural sources. The incorporation of CQD effectively enhanced the supercapacitive performance of NiS by leveraging their exceptional electron transport properties and surface functionalities, which facilitated improved charge-transfer kinetics and structural stability. However, its electrochemical performance is still not very satisfactory. On the other hand, ZnS QDs have been extensively studied in various fields, like light-emitting diodes and solar cells, because of their chemical and thermal stability [19]. ZnS QDs exhibit exceptional structural stability, high surface-to-volume ratios, and quantum confinement effects that enhance electron transport. Their nanoscale dimensions facilitate intimate interfacial contact with CeS<sub>2</sub>, mitigating particle aggregation and shortening ion diffusion paths—critical for improving rate capability. While ZnS QDs alone exhibit low specific capacitance due to limited redox activity, their integration with high-capacity materials like CeS<sub>2</sub> can leverage synergistic effects. In addition, their low production cost enable them to be used in a wider range of applications [14]. The combined interaction of the two materials causing a synergistic effect may result in enhanced electrochemical performance of the composite [18]. To the best of our knowledge, the composite material of CeS<sub>2</sub> and ZnS, i.e., CeS<sub>2</sub>/ZnS QD nanocomposites have not been reported in the literature as a material for supercapacitor applications.

In this study, we synthesized a series of CeS<sub>2</sub>/ZnS QD nanocomposites with varying ZnS QD ratios via a hydrothermal method, aiming to enhance the electrochemical performance of CeS<sub>2</sub>-based supercapacitor electrodes. For the first time, the synergistic effects of CeS<sub>2</sub> (high theoretical capacitance) and ZnS QDs (structural stability and conductivity) were systematically investigated. Structural characterization (XRD, SEM, TEM) confirmed the successful formation of a heterostructure, where ZnS QDs (cubic sphalerite phase) were uniformly dispersed on CeS<sub>2</sub> nanospheres, mitigating particle aggregation and shortening ion diffusion paths.

## 2. Experimental Section

### 2.1. Materials Synthesis

Cerium nitrate hexahydrate ( $\text{Ce}(\text{NO}_3)_3$ , 99.99%), Sodium sulfide ( $\text{Na}_2\text{S}$ , 98%), and Zinc acetate dihydrate ( $\text{C}_4\text{H}_6\text{O}_4\text{Zn 2H}_2\text{O}$ , 99.99%) were bought from Aladdin Chemical Co., Ltd. Shanghai, China. Glutathione reduced ( $\text{C}_{10}\text{H}_{17}\text{N}_3\text{O}_6\text{S}$ , 98%), Isopropyl alcohol ( $\text{C}_3\text{H}_8\text{O}$ , 99.5%) Sodium hydroxide and Ethyl alcohol were sourced from Energy Chemical. Conductive carbon black (C, 99.5%) was bought from Zesheng Scientific Co., Ltd. Anhui, China. Activated carbon (AC, the electrochemical behavior of AC can be seen in Figure S1) was bought from Shenze Chemical Technology Co., Ltd. Shanghai, China. All the chemicals were of analytical grade and utilized without any additional purification.

### 2.2. Synthesis of $\text{CeS}_2$

$\text{CeS}_2$  nanoparticles were synthesized via a hydrothermal method. Specifically, a 0.1 M  $\text{Na}_2\text{S}$  solution was gradually introduced into a 0.5 M  $\text{Ce}(\text{NO}_3)_3$  solution under continuous magnetic stirring. Following thorough mixing for 30 min, the resulting precursor solution was transferred into a 100 mL Teflon-lined stainless steel autoclave, filled to 70% of its volume. The autoclave was then subjected to hydrothermal treatment at 180 °C for 14 h. Upon completion, the system was allowed to cool naturally to ambient temperature. The precipitated product was subsequently washed multiple times with deionized water and ethanol to remove residual impurities. Finally, the purified  $\text{CeS}_2$  nanoparticles were dried under vacuum at 60 °C overnight [16].

### 2.3. Synthesis of $\text{ZnS}$ QD

$\text{ZnS}$  quantum dots (QDs) were synthesized via a coprecipitation method using glutathione (GSH) as a capping agent. Initially, 0.1 M GSH was dissolved in 10 mL of DDW, while 0.1 M zinc acetate ( $\text{Zn}(\text{CH}_3\text{COO})_2$ ) was separately dissolved in another 10 mL of DDW. The zinc acetate solution was then added dropwise to the GSH solution under continuous stirring in a nitrogen atmosphere. The pH of the mixture was adjusted to 10.5 using 1.0 M NaOH to clarify the solution by eliminating turbidity. After stirring for 30 min, 10 mL of 0.1 M sodium sulfide ( $\text{Na}_2\text{S}$ ) solution was introduced, and the reaction was allowed to proceed for an additional 20 min under nitrogen. Subsequently, the solution temperature was raised to 100 °C and maintained for 2 h. The resulting product was precipitated by the addition of isopropanol and collected by centrifugation at 6000 rpm for 20 min. The obtained  $\text{ZnS}$  QD powder was dried overnight in a vacuum oven at 40 °C. Glutathione acted as a stabilizing ligand, preventing agglomeration and ensuring colloidal stability of the  $\text{ZnS}$  quantum dots in aqueous media [17].

### 2.4. Synthesis of $\text{CeS}_2/\text{ZnS}$ QD Nanocomposite

The  $\text{CeS}_2/\text{ZnS}$  QD nanocomposite was synthesized via a hydrothermal-assisted precipitation method. Initially, 0.1 M  $\text{Ce}(\text{NO}_3)_3$  was dispersed into the  $\text{ZnS}$  QDs solution and stirred magnetically for 30 min. Subsequently, 0.5 mmol of  $\text{Na}_2\text{S}$  was added as the precipitating agent under continuous stirring. The resulting mixture was transferred into a 100 mL Teflon-lined stainless steel autoclave and subjected to hydrothermal treatment at 180 °C for 14 h in a preheated furnace. After the reaction was complete, the vessel was allowed to cool naturally to room temperature. The product was then collected by centrifugation and washed three times with deionized water and anhydrous ethanol to remove impurities. Finally, the obtained nanoparticles were dried overnight in a vacuum oven at 60 °C. To systematically investigate the effect of composition on electrochemical performance, five distinct samples were synthesized and prepared for electrochemical

testing: pure CeS<sub>2</sub> (denoted as 1:0), CeS<sub>2</sub>/ZnS QD composites with molar ratios of 2:1, 1:1, and 1:2 (CeS<sub>2</sub>:ZnS QD), and pure ZnS QD (denoted as 0:1).

### 2.5. Electrode Preparation

Electrochemical performance was evaluated using a three-electrode system in 1 M KOH electrolyte. The working electrode was fabricated by combining 16 mg of active material, 2 mg of conductive carbon black, and 2 mg of polyvinylidene fluoride (PVDF). Subsequently, 6–8 drops of N-methylpyrrolidone (NMP) were added to the thoroughly homogenized mixture, which was then ground for 30 min. The mixture was applied to a (1 × 1 cm<sup>2</sup>) area on the nickel foam and dried in an oven at a set temperature of 60 °C for 12 h. The weight of the active material coated on each sheet electrode was kept around 2 mg and used a pre-prepared 3 M KOH aqueous solution as electrolyte during the test.

## 3. Characterization

### 3.1. Morphological and Structural Characterization

The crystallinity and phase purity of the prepared composites were analyzed using X-ray diffraction (XRD, D/max2550VB/PC, Rigaku Corporation Akishima-Shi, Tokyo, Japan). Morphological studies were performed using scanning electron microscopy (SEM, S-3400, Hitachi, Ltd., Tokyo, Japan) and transmission electron microscopy (TEM, JEL-2100, Hitachi, Ltd.).

### 3.2. Electrochemical Characterizations

Electrochemical measurements, including cyclic voltammetry (CV), galvanostatic charge–discharge (GCD), and electrochemical impedance spectroscopy (EIS), were conducted using a conventional three-electrode configuration. The working electrode was prepared by loading 2 mg of the active material onto nickel foam. A platinum wire served as the counter electrode, and a Ag/AgCl electrode was employed as the reference electrode. All measurements were carried out in a 3 M KOH aqueous electrolyte.

All electrochemical analyses were conducted at room temperature using an electrochemical workstation (CS-150M, KST Instrument Co., Ltd., Wuhan, China). These techniques offer complementary insights and are extensively employed in the characterization of electrode materials. Cyclic voltammetry (CV) measurements were performed at scan rates ranging from 5 to 40 mV/s. GCD tests were carried out at current densities between 1 and 20 A/g. Electrochemical impedance spectroscopy (EIS) was conducted over a frequency range of 10<sup>-2</sup> Hz to 10 kHz. The specific capacitance ( $C_s$ ) values were derived from the CV curves according to Equation (1) [20].

$$C_s = \int \frac{Idv}{sm\Delta V} \quad (1)$$

where  $I$  is current and  $dv$  is the voltage differential during the cyclic voltammetry,  $m$  is the mass loading of active material,  $s$  is the scan rate, and  $\Delta V$  is the potential window. The  $C_s$  of the electrode materials from the GCD curve were calculated using Equation (2) [21].

$$C_s = \frac{Idt}{m\Delta V} \quad (2)$$

where  $I$ ,  $dt$ ,  $m$  and  $\Delta V$  denote the discharge current, discharge time, mass of the active material, and potential window during the discharge process, respectively. Equations (3) and (4) are subsequently employed to quantitatively determine the energy density and power den-

sity of the electrode materials, providing critical metrics for evaluating their electrochemical performance [22].

$$E = \frac{C_s \Delta V^2}{7.2} \quad (3)$$

$$P = \frac{E \times 3600}{t} \quad (4)$$

where  $C_s$ ,  $\Delta V$  and  $t$  represent the specific capacitance, the potential window during the discharge phase, and the discharge time, respectively.

## 4. Results and Discussion

### 4.1. Structural and Morphological Analysis

Figure 1 presents the XRD pattern of the synthesized sample. The peaks of the XRD spectra of pure  $\text{CeS}_2$  are reflected at  $22.38^\circ$ ,  $27.49^\circ$ ,  $32.99^\circ$ ,  $37.71^\circ$ , and  $45.31^\circ$ , which correspond well to the values given in the International Centre for Diffraction Data (ICDD) standard card ICDD 075-1109 (ICDD 1) [23]. The XRD spectrum of the pure ZnS quantum dots corresponds well with the standard card ICDD 77-2100 (ICDD 2) [24], with three characteristic peaks at  $2\theta$  of  $28.88^\circ$ ,  $47.55^\circ$ , and  $56.46^\circ$ , corresponding to the crystallographic planes (111), (220), and (311), respectively, which are the main peaks denoting the cubic zinc sphalerite structure of the ZnS quantum dots. Comparative analysis of the obtained composite results with the ICDD card library shows the presence of both  $\text{CeS}_2$  (ICDD 1) as well as ZnS QD (ICDD 2) in the  $\text{CeS}_2$ /ZnS QD samples, and the diffraction peaks correspond to either the  $\text{CeS}_2$  or ZnS QD compositions with no additional peaks, thus supporting the  $\text{CeS}_2$ /ZnS QD composite structure formation.

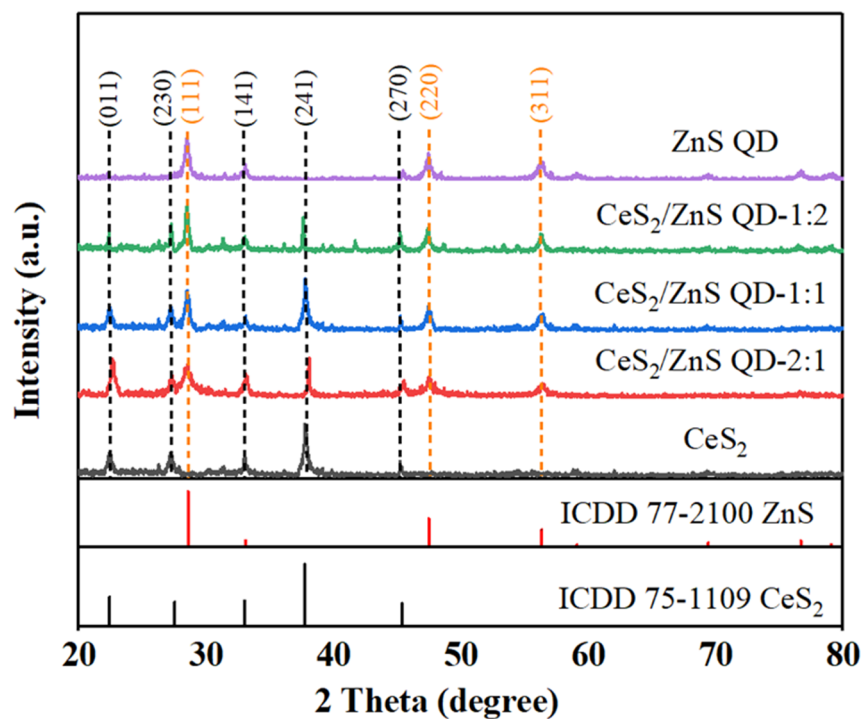


**Figure 1.** XRD patterns of the  $\text{CeS}_2$ , ZnS QD and  $\text{CeS}_2$ /ZnS QD composite.

FE-SEM images of  $\text{CeS}_2$ ,  $\text{CeS}_2$ /ZnS QD-1:1, and ZnS QD are shown in Figure 2a–c, respectively.  $\text{CeS}_2$  (Figure 2a) shows large clusters of irregular shapes, with a minimal amount of scattered nanoparticles, while the ZnS QD particles in Figure 2b,c are of minimal particular shape. As can be discerned from the figure, the  $\text{CeS}_2$  clusters are composed of irregular nanoparticles, with cluster sizes ranging approximately from 500 nm to

1100 nm. Figure 2b is the image of the CeS<sub>2</sub>/ZnS QD-1:1 sample. The red arrows point to a CeS<sub>2</sub>-like cluster and the blue arrows point mainly to ZnS QDs. It can be seen from the figure that the size of the CeS<sub>2</sub>-like cluster has significantly decreased. This is because the heterogeneous component (ZnS QD) introduced during the compounding process provides more cluster nucleation sites, resulting in an increase in the number of clusters, dispersing the material agglomeration paths, and inhibiting the excessive growth of a cluster. The shapes of pure ZnS QD particles (Figure 2c) are also irregular nanoparticles, and the particle size is approximately in the 100 nm range.

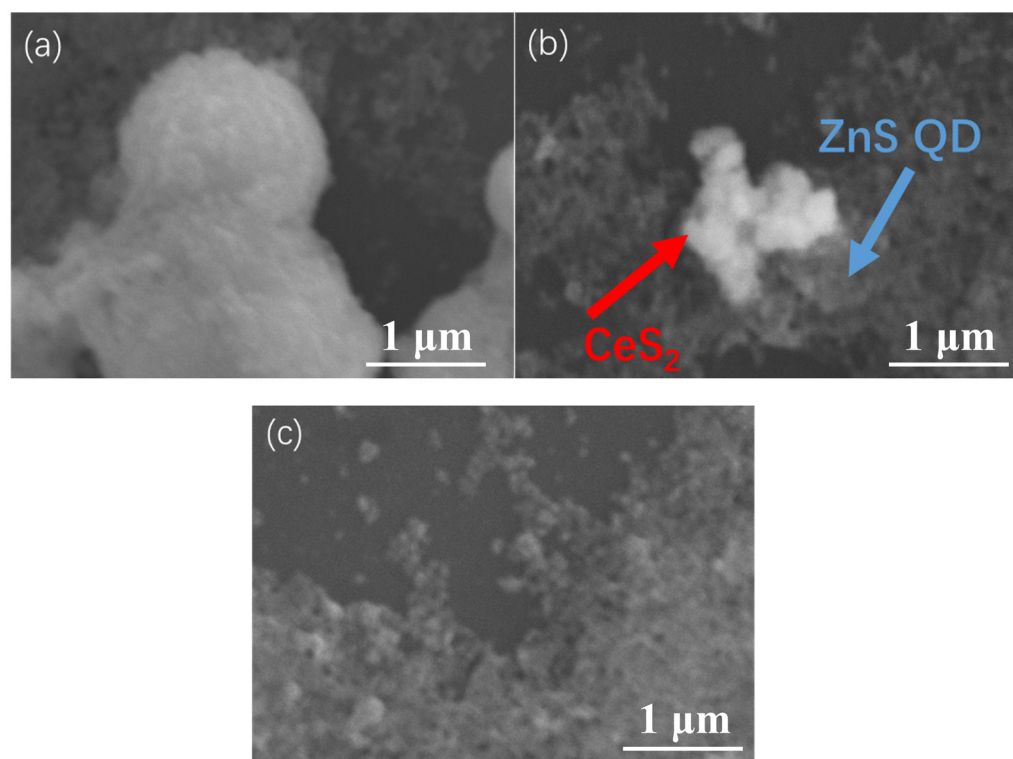


**Figure 2.** FE-SEM patterns of the samples: (a) CeS<sub>2</sub>, (b) CeS<sub>2</sub>/ZnS QD-1:1, and (c) ZnS QD.

For deeper insight into the material's microscopic morphology and crystal structure, high-resolution transmission electron microscopy (HRTEM) analysis was performed, with the findings presented in Figure 3. Figure 3a,b demonstrate that the composite cluster actually consisted of nanoparticles of CeS<sub>2</sub> as well as ZnS quantum dots. Figure 3c (Yellow Box) displays lattice fringes with a spacing of 0.271 nm, corresponding to the (200) crystallographic plane of cubic ZnS. This confirms the presence of well-crystallized ZnS QDs in the composite. Figure 3d (Blue Box) shows lattice fringes with a spacing of 0.324 nm, assigned to the (230) plane of CeS<sub>2</sub>. This verifies the retention of CeS<sub>2</sub>'s crystalline structure after composite formation. Figure 3e (orange Box) reveals an interfacial region where lattice fringes of both CeS<sub>2</sub> ((0.235 nm, (241)) and ZnS ((0.312 nm, (111)) coexist, indicating heterojunction formation. This intimate contact between CeS<sub>2</sub> and ZnS QDs facilitates efficient charge transfer, corroborating the enhanced electrochemical performance. These observations collectively demonstrate the successful integration of CeS<sub>2</sub> and ZnS QDs into a heterostructured composite, where ZnS QDs mitigate CeS<sub>2</sub> agglomeration and improve ion diffusion kinetics. In addition, the presence of both CeS<sub>2</sub> and ZnS diffraction rings in the SAED image (Figure 3f) indicates the presence of CeS<sub>2</sub> and ZnS QDs.

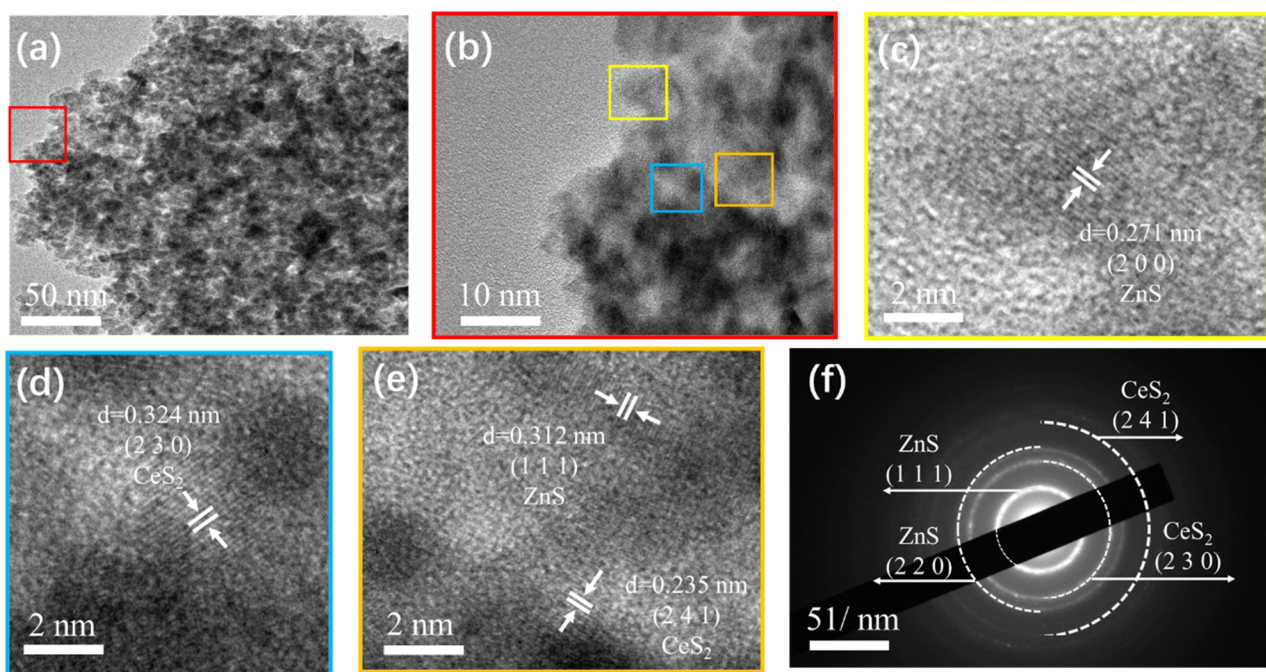


**Figure 3.** TEM image of CeS<sub>2</sub>/ZnS QD-1:1: (a) TEM image of the composite material, (b) the area in the red box in Figure a, (c) the area in the yellow box in Figure b, (d) the blue box area in Figure b, (e) the area in the orange box in Figure b, (f) SAED diffraction image.

It would be interesting to study the nano-pore distribution and surface area of CeO<sub>2</sub>/ZnS composite material. The nitrogen adsorption and desorption has been conventionally studied for activated carbon supercapacitor materials [25,26], but for CeO<sub>2</sub>/ZnS composite material in this study, its specific surface area and nitrogen adsorption capacity are significantly lower than those of the nano-porous activated carbon materials, and there is difficulty in analyzing the pore distributions [27,28]. Further research will be conducted to better analyze and determine these properties of the metal compound composite materials in the future.

#### 4.2. Electrochemical Studies

To analyze the effect of the variation in the added ZnS QD ratio on the electrochemical properties of the composites, the series of samples were tested in a three-electrode system for electrochemical performance, and the results are shown in Figure 4. CV curves (Figure 4a–e) recorded at scan rates of 5 to 40 mV/s and the voltage window of 0 V to 0.5 V revealed distinct redox peaks for all samples, confirming pseudocapacitive behavior.

The observed Faradaic peaks unequivocally demonstrate the battery-type electrochemical behavior of the material. For the pristine CeS<sub>2</sub> sample, distinct cathodic and anodic peaks were recorded at 0.40 V and 0.24 V, respectively, corresponding to reversible redox reactions. Upon formation of the CeS<sub>2</sub>/ZnS quantum dot composite, these redox peak potentials shifted toward lower values, indicative of altered electrochemical kinetics and enhanced charge-transfer processes within the heterostructured material. This suggests that, relative to individual materials, electrodes made from composite materials exhibit a more rapid and reversible charge-transfer process. CV reflects the energy storage reaction mechanism of Ce reducing from the oxidation state of +4 to +3, in which electrons are involved in the redox process. Meanwhile, we found that as the scanning rate increased, the positions of the redox peaks shifted to varying degrees. Due to the high kinetic energy, the resistance of the ions would increase, and their interaction time with the electrode surface was the shortest, thus the specific capacitance value was relatively low. The CeS<sub>2</sub>/ZnS QD-

1:1 composite (Figure 4c) exhibited the highest peak currents, indicating superior charge storage capacity. A comparative CV plot and GCD plot that overlays the performance of all materials at 5 mV/s and 1 A/g is shown in Figure S2. Meanwhile, its wide redox peak suggests a multi-step reaction or surface adsorption process. Even at a high sweep rate (40 mV/s), the peak shape does not undergo obvious distortion, suggesting rapid charge-transfer kinetics.

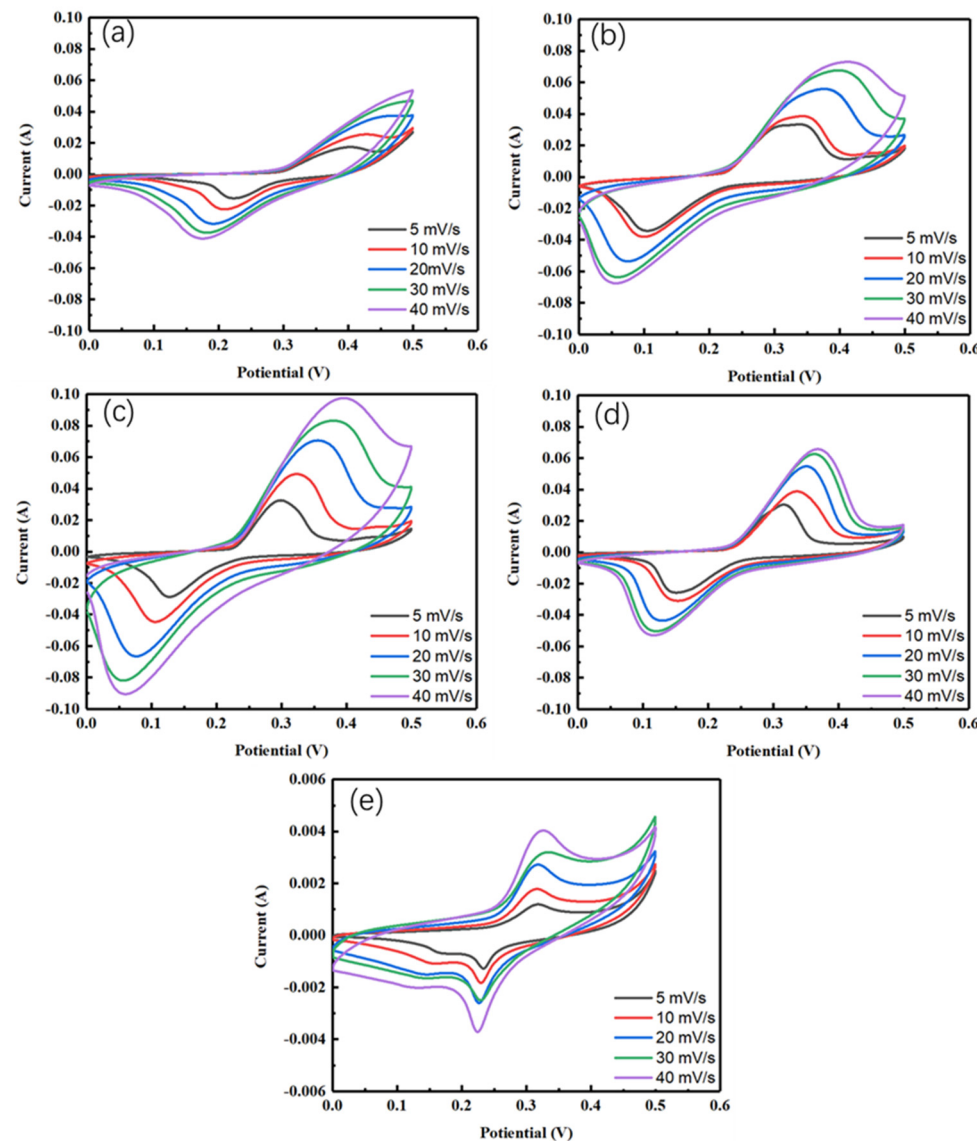


**Figure 4.** CV curves at 5, 10, 20, 30, and 40 mV/s for samples with different composite ratios, (a)  $\text{CeS}_2$ , (b)  $\text{CeS}_2/\text{ZnS}$  QD-2:1, (c)  $\text{CeS}_2/\text{ZnS}$  QD-1:1, (d)  $\text{CeS}_2/\text{ZnS}$  QD-1:2, (e)  $\text{ZnS}$  QD.

An important observation in practical supercapacitor studies is that the cyclic voltammetry (CV) curves of most supercapacitor materials often differ from the ideal rectangular shape characteristic of an ideal capacitor, a phenomenon observed across all classes of supercapacitive materials, including electric double-layer capacitor materials (EDLCs) and generalized pseudocapacitive materials (which can be further divided into specialized pseudocapacitive materials and battery-type materials). And there is the debate regarding the classification of battery-type materials within the supercapacitor framework [29]. While some people argue that battery-type materials should be excluded from the supercapacitor category due to their noncapacitive CV signatures, counterarguments emphasize their significant capacitive contributions during charge storage and their superior power den-

sities compared to conventional battery materials. A possible approach to avoid such a controversy would be to adopt the broader term “electrochemical energy storage materials”; however, many experts recommend describing it more specifically, e.g., as energy storage materials for supercapacitor devices. Ultimately, the primary research objective should focus on developing advanced materials that synergistically combine high energy density, power density, and cycling stability, regardless of strict taxonomic boundaries [30], instead of suppressing different opinions.

GCD measurements were conducted to further quantify the specific capacitance and assess the applicability of the nanomaterials as supercapacitor electrodes. The characteristic nonlinear, bending profile of the GCD curves confirms the pseudocapacitive behavior of the nanomaterials, which is consistent with the redox features observed in the cyclic voltammetry (CV) analysis. As the current density increases, the specific capacitance decreases for all materials. This reduction is attributed to the increased resistance of electrolyte ions at higher current densities. Meanwhile, the three composite materials with different proportions (Figure 5b–d) all have multiple platforms, suggesting that the materials undergo multiple steps of reaction, which is consistent with the conclusion of the CV curve. Even at 20 A/g, the composite retained 55 F/g, demonstrating excellent rate capability.

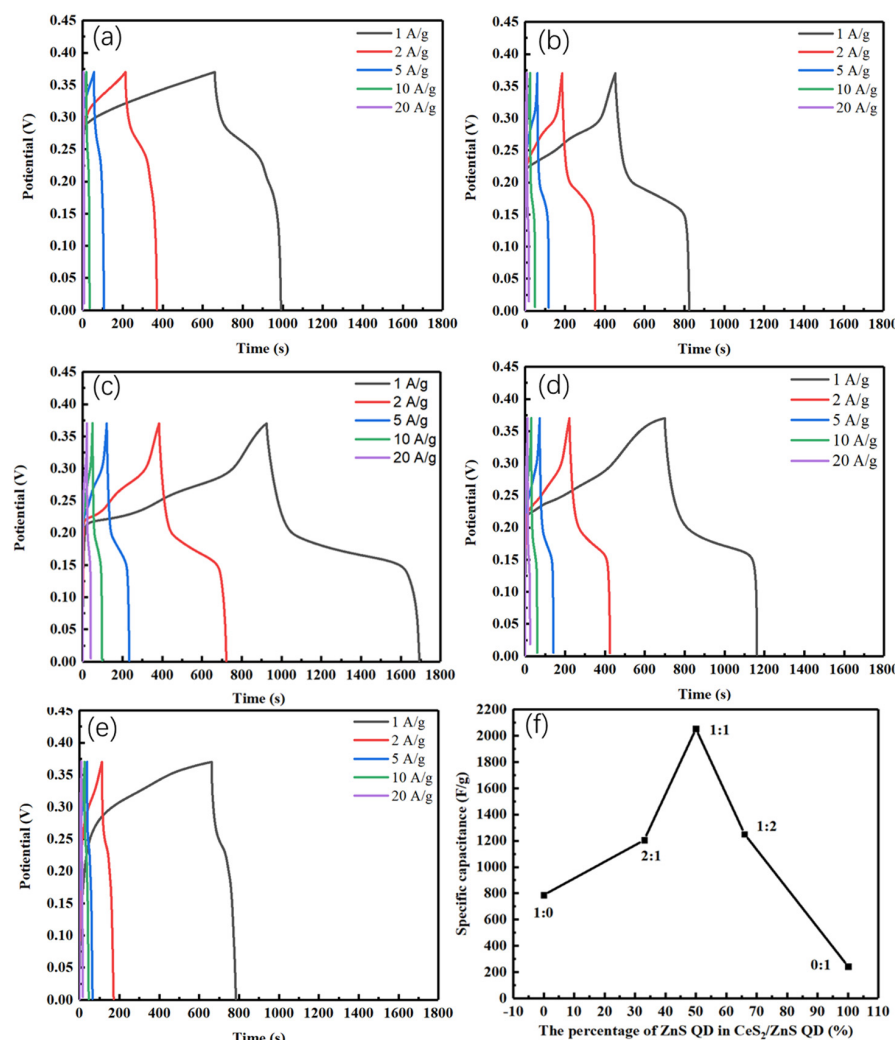


**Figure 5.** GCD curves at 1, 2, 5, 10, and 20 A/g for samples with different composite ratios, (a) CeS<sub>2</sub>, (b) CeS<sub>2</sub>/ZnS-2:1, (c) CeS<sub>2</sub>/ZnS QD-1:1, (d) CeS<sub>2</sub>/ZnS QD-1:2, (e) ZnS QD, (f) Trend chart of specific capacitance at 1 A/g for samples with different molar ratios.

The specific electrochemical reactions related to redox peaks are as follows:



The surface of quantum dots is rich in active sites, and the functional groups on the surface can adsorb reactants and promote electron transfer [31]. On the other hand, quantum dots can lift electrons to the conduction band by applying light or electric field, thereby exhibiting reducing properties in redox reactions [32]. The high-density unsaturated bonds on the surface of the quantum dot capture electrons/holes and directly take part in reduction reactions [33].

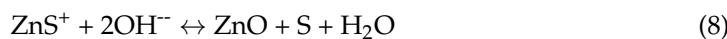


Figure 5f depicts the variation in specific capacitance as a function of ZnS quantum dot (QD) content. At 0% ZnS QD, the pure  $\text{CeS}_2$  material exhibits a specific capacitance of 780 F/g at a current density of 1 A/g. This relatively low value is attributed to the limited conductivity and insufficient active sites of the pristine  $\text{CeS}_2$ , resulting in suboptimal coulombic efficiency and energy storage performance. Upon increasing the ZnS QD content to 50%, the specific capacitance and coulombic efficiency reach their maximum values, with a peak capacitance of 2054 F/g at 1 A/g (specific capacity of 256 mAh/g). In contrast, at 100% ZnS QD content, the specific capacitance markedly decreases to approximately 242 F/g at 1 A/g (specific capacity of 30 mAh/g), accompanied by a significant decline in coulombic efficiency. A comparative GCD plot overlaying the performance of all samples at 1 A/g is provided in Figure S2. Additionally, specific capacitance values for all samples across varying current densities are summarized in Table 1.

**Table 1.** Specific capacitance values of  $\text{CeS}_2/\text{ZnS}$  QD composite with different proportions (F/g).

| Current Density (A/g) | $\text{CeS}_2$ | $\text{CeS}_2/\text{ZnS}$ QD-2:1 | $\text{CeS}_2/\text{ZnS}$ QD-1:1 | $\text{CeS}_2/\text{ZnS}$ QD-1:2 | ZnS QD |
|-----------------------|----------------|----------------------------------|----------------------------------|----------------------------------|--------|
| 1                     | 780            | 1205                             | 2074                             | 1250                             | 242    |
| 2                     | 346            | 595                              | 935                              | 690                              | 128    |
| 5                     | 110            | 226                              | 306                              | 240                              | 48     |
| 10                    | 42             | 92                               | 131                              | 105                              | 22     |
| 20                    | 14             | 40                               | 55                               | 48                               | 11     |

The electrochemical test of the  $\text{CeS}_2/\text{ZnS}$  QD-1:1 sample with the best electrical performance was further improved. Figure 6a presents the specific capacitance of the sample measured at different current densities ranging from 1 A/g to 20 A/g, with the values calculated using Equation (2).

At a low current density of 1 A/g, the  $\text{CeS}_2/\text{ZnS}$  QD (1:1) electrode achieves a high specific capacitance of 2054 F/g, demonstrating the material's outstanding charge storage capability. This is because of the combination of  $\text{CeS}_2/\text{ZnS}$  QD. ZnS QD inhibits the aggregation of  $\text{CeS}_2$ , which was also reflected in the previous FESEM scan images. Reducing the inherent resistivity can greatly reduce the resistance of  $\text{CeS}_2$  and improve energy conversion efficiency. In addition, for the  $\text{CeS}_2/\text{ZnS}$  QD composite,  $\text{CeS}_2$  can undergo more redox reactions on the surface of ZnS QD, thereby increasing the specific capacitance of the composite material. Meanwhile, for the  $\text{CeS}_2/\text{ZnS}$  QD composite, the synergistic effect between Ce ions and Zn ions results in a higher specific capacitance value of the composite material. The synergistic effect significantly enhances the specific capacitance of supercapacitors by optimizing electron transport, increasing active sites and stabilizing the

structure [34,35]. The EIS impedance spectrum of the CeS<sub>2</sub>/ZnS QD-1:1 sample was tested in Figure 6b. The intercept of the high-frequency region with the real axis corresponds to the equivalent internal resistance ( $R_s$ ) of the material. After amplification, the equivalent internal resistance of CeS<sub>2</sub>/ZnS QD-1:1 was measured to be 0.31 Ω. The equivalent internal resistance of the composite material is very small, indicating that a heterogeneous structure is formed between the two materials, which greatly reduced the internal resistance of the materials and thereby improved the electrochemical performance of the composite material. In addition, the electron transfer efficiency of the material is related to the circular radius in the high-frequency region. The composite material CeS<sub>2</sub>/ZnS QD-1:1 shows almost no semi-circular region, which once again indicates that the electron transfer efficiency of the composite material is relatively high. Figure 6c tested the cycling stability of a single electrode of the composite material CeS<sub>2</sub>/ZnS QD-1:1 for 3000 cycles. The specific capacitance of the composite material CeS<sub>2</sub>/ZnS QD-1:1 slightly increased after 100 cycles, indicating that the material was activated. Subsequently, with the increase in cycles at this time, the specific capacitance retention rate was 65.1%, demonstrating good long-term electrochemical stability. Figure 6d tests the coulombic efficiency curve of the composite material CeS<sub>2</sub>/ZnS QD-1:1. The black curve and the red curve in the figure represent the charging capacity curve and the discharging capacity curve, respectively.

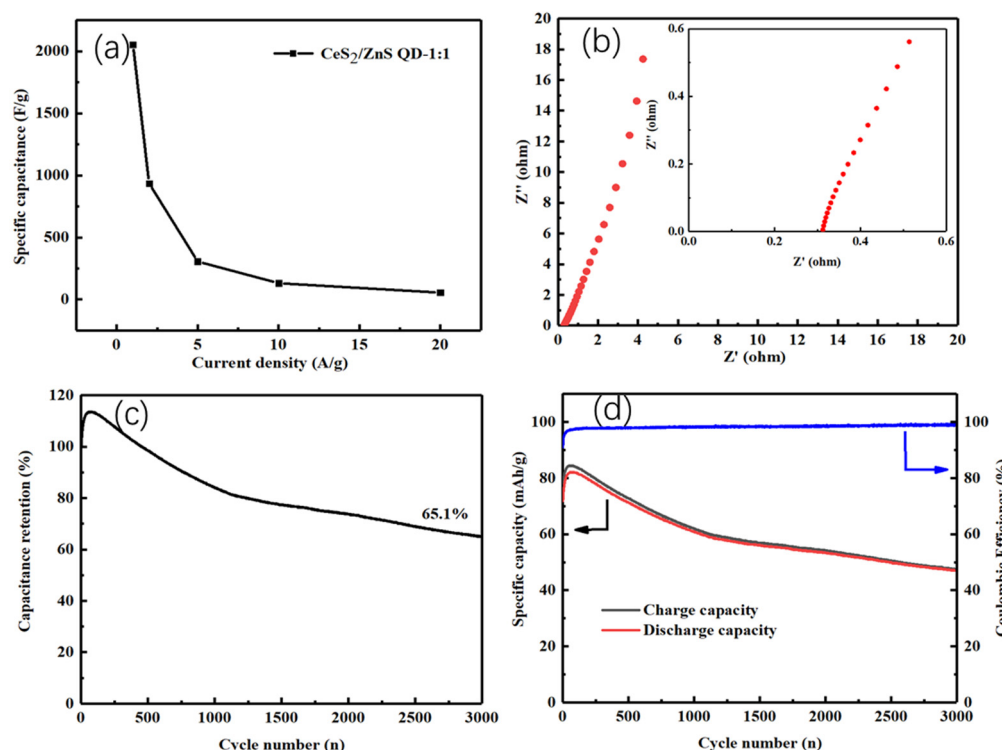


**Figure 6.** Electrochemical properties of CeS<sub>2</sub>/ZnS QD-1:1: (a) specific capacitance values at different current density, (b) EIS graph, embedded graph: enlarged image of the high-frequency region, the red dots are experimental data points of impedance characterization (c) cyclic performance, (d) coulomb efficiency, calculated according to Equation (9) [36].

$$CE = \frac{(Charge\ capacity)}{(Discharge\ capacity)} \times 100\% \quad (9)$$

According to the calculation, the coulombic efficiency (blue curve) of the composite material CeS<sub>2</sub>/ZnS QD-1:1 increased from 92% at the beginning of 100 cycles to 98% in the later stage of the cycle, indicating that the side reactions of the material were very few and the charge and discharge processes were highly reversible. In addition, we can find

that the gray weight and the red curve decrease simultaneously, and the ratio is stable, indicating that the capacity loss is due to the loss of active material rather than the reduction in coulombic efficiency. As evidenced by structural and electrochemical data, the proposed synergistic mechanism may involve three key effects. (1) Enhanced Charge Transfer via Heterojunction Formation: The TEM/SAED results (Figure 3) confirm the contact between CeS<sub>2</sub> and ZnS QDs, forming heterostructure. The lattice spacing of CeS<sub>2</sub> (0.324 nm, (230)) and ZnS (0.271 nm, (200)) creates interfacial strain, which induces localized electric fields at the heterojunction [34]. This facilitates electron transfer from CeS<sub>2</sub> to ZnS QDs during redox reactions, reducing charge-transfer resistance (0.31 Ω, Figure 6b). (2) Mitigation of Aggregation and Increased Active Sites: SEM (Figure 2b) reveals that ZnS QDs act as spacers, preventing CeS<sub>2</sub> particle aggregation and exposing more electroactive surfaces. The composite's higher specific capacitance (2054 F/g vs. 787 F/g for pure CeS<sub>2</sub>) aligns with its larger electrochemically active area. (3) Stabilization of Redox Chemistry: The ZnS QDs' surface functional groups (e.g., -SH from glutathione capping) adsorb OH<sup>-</sup> ions from the electrolyte, promoting the reversible Ce<sup>3+</sup>/Ce<sup>4+</sup> transition (Equation (5)) while suppressing dissolution. This is reflected in the composite's high coulombic efficiency (98%, Figure 6d) and cycling stability (84% retention after 10,000 cycles, Figure 7e).

To investigate the practical application potential of the CeS<sub>2</sub>/ZnS QD (1:1) electrode material, asymmetric supercapacitor devices were fabricated using the CeS<sub>2</sub>/ZnS QD (1:1) composite as the positive electrode and activated carbon (AC) as the negative electrode. A series of tests were performed on the devices, with the results presented in Figure 7. Figure 7a compares the CV curves of CeS<sub>2</sub>/ZnS QD (1:1) and AC at a scan rate of 20 mV/s. It is evident that the two materials display distinctly different capacitive behaviors, along with notable variations in their voltage ranges. The voltage range of commercial activated carbon is −1.0–0 V, and the voltage range of CeS<sub>2</sub>/ZnS QD-1:1 is 0–0.5 V. Taking 0–1.5 V as the working voltage range of the device CV, the CV test results are shown in Figure 7b. It can be found that the curve shows redox peaks and also retains a quasi-rectangular shape, indicating that both the double-layer capacitance contributed by activated carbon and the pseudocapacitance contributed by CeS<sub>2</sub>/ZnS QD-1:1 exist simultaneously. Meanwhile, at a higher scanning rate, the shape of the CV curve does not show obvious deformation, indicating that the charge-transfer rate is relatively fast. The charge–discharge curves of the CeS<sub>2</sub>/ZnS QD-1:1//AC device are shown in Figure 7c. The charge–discharge times of the material at low current density (1 A/g) are almost equal, indicating that this device has excellent coulombic efficiency. This shows that it has an excellent energy storage effect at a low current density and has certain practical application value. When the set current density gradually increases to 10 A/g, there is a voltage lag between the charging and discharging curves. This is due to the existence of a resistance voltage drop (IR drop). During the charging process, the internal resistance (IR) of the battery leads to a higher charging voltage, which means that a greater voltage must be applied to complete the same charging process. When the battery transitions from charging to discharging, due to the existence of internal resistance within the battery, the discharge voltage drops immediately, resulting in a significant decrease in capacitance [37,38]. The specific capacitance of the device was calculated based on the GCD curve and Equation (2), and the result is shown in Figure 7d. The specific capacitance of the device is 242 F/g at 1 A/g (specific capacity of 107 mAh/g). Figure 7e tested 10,000 charge–discharge cycles of the device at 10 A/g. The attenuation was relatively fast in the first 2000 cycles, and it tended to be stable in the later stage. After cycling, the device retained 84% of its initial specific capacitance, demonstrating excellent long-term cycling stability. According to Equations (3) and (4), the energy density of the material at different power densities was calculated. The data obtained were plotted as an energy density versus power density curve (Ragone plot), as

shown in Figure 7f. The device exhibited an energy density of 77 Wh/kg at a low power density of 710 W/kg and retained a substantial energy density of 12 Wh/kg even at a high power density of 7100 W/kg. These outstanding energy storage performances surpass those reported for most cerium-based and quantum dot-based supercapacitor systems in the current literature, demonstrating the superior electrochemical capabilities of the developed nanocomposite electrode.

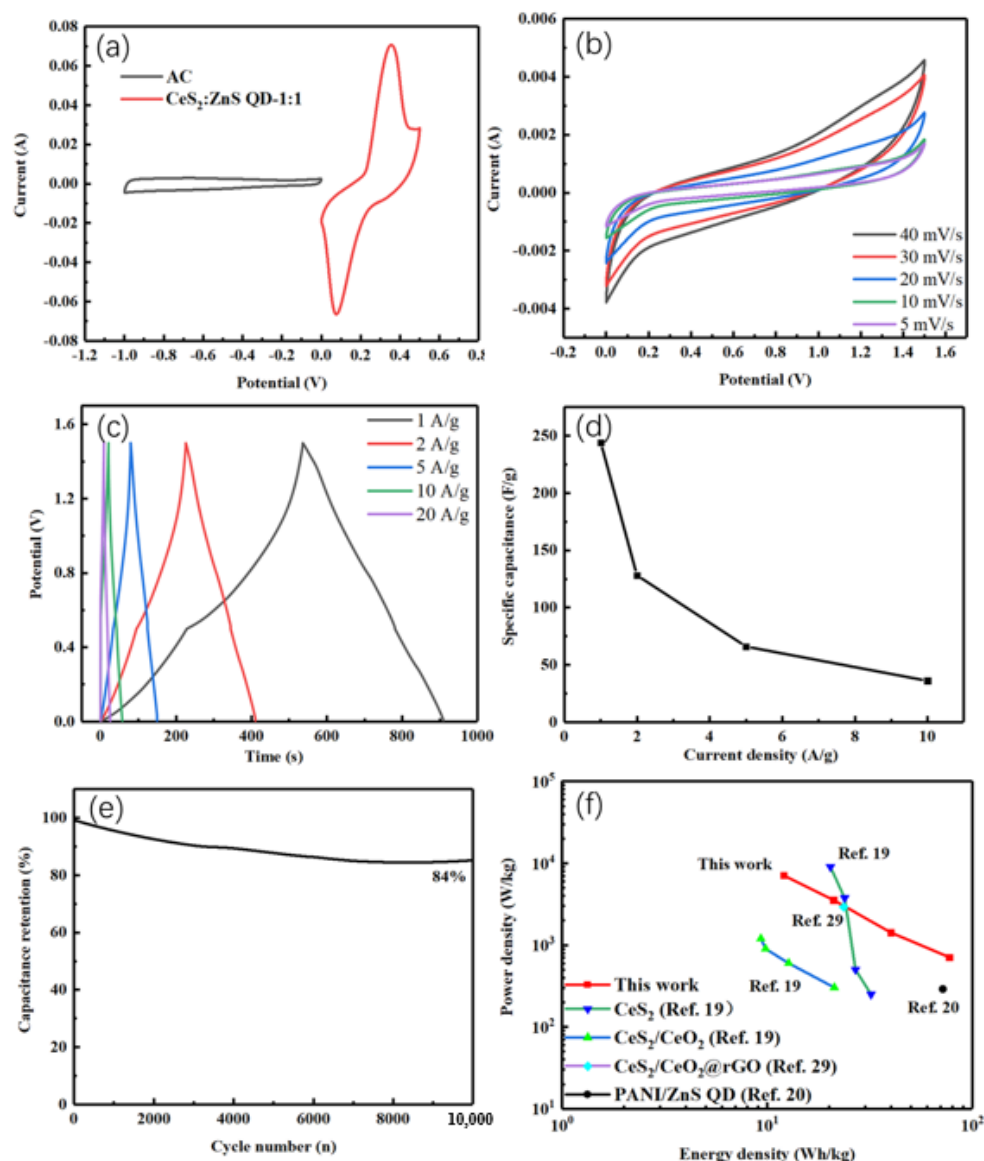


**Figure 7.** Electrochemical performance of the CeS<sub>2</sub>/ZnS QD-1:1//AC: (a) CV curves of the CeS<sub>2</sub>/ZnS QD-1:1 and AC at 20 mV/s, (b) CV curves, (c) GCD curves, (d) rate performance of the CeS<sub>2</sub>/ZnS QD-1:1//AC, (e) cycle properties, (f) energy density–power density Ragone plot.

## 5. Conclusions

In conclusion, we prepared CeS<sub>2</sub>/ZnS QD samples in different proportions using a simple hydrothermal synthesis method. The composite's unique architecture, ZnS QDs uniformly anchored on CeS<sub>2</sub> nanospheres was confirmed by XRD and TEM characterizations. This design provided abundant active sites, enhanced conductivity, and mitigated aggregation. The heterostructure of CeS<sub>2</sub>/ZnS QD significantly improved the electrochemical performance. The CeS<sub>2</sub>/ZnS QD-1:1 composite achieved a remarkable specific capacitance of 2054 F/g at 1 A/g. It showed low charge-transfer resistance (0.31 Ω) and high coulom-

bic efficiency (98%). The assembled asymmetric supercapacitor ( $\text{CeS}_2/\text{ZnS QD-1:1} // \text{AC}$ ) delivered an energy density of 77 Wh/kg at 710 W/kg and retained 84% capacitance after 10,000 cycles. By utilizing this innovative composite, the material's specific surface area is effectively increased, ion transport rates are accelerated, and the composite's specific capacitance is markedly enhanced. This work not only advances the design of sulfide/QD hybrids but also provides a strategy that could help further enhance the performance of other QD-based electrochemical energy storage materials.

**Supplementary Materials:** The following supporting information can be downloaded at <https://www.mdpi.com/article/10.3390/batteries11080289/s1>, Figure S1. Electrochemical behavior of commercial activated carbon (AC): (a) CV curves, (b) GCD curves, (c) rate plot. Figure S2. (a) CV curves at 5 mV/s for samples with different composite ratios, (b) GCD curves at 1 A/g for samples with different composite ratios.

**Author Contributions:** S.-D.X.: writing—original draft, methodology, and data curation. L.-C.W.: writing—data curation and editing. M.A.: writing—review and editing. X.C.: methodology, writing—original draft, formal analysis, and supervision. L.-F.S.: resources and data curation. Z.-Y.Z.: data curation and validation. K.X.: data curation and validation. All authors have read and agreed to the published version of the manuscript.

**Funding:** This work was supported by the National Natural Science Foundation of China (21875066); Shanghai Leading Academic Discipline Project (B502); and the Shanghai Key Laboratory Project (08DZ2230500).

**Data Availability Statement:** The data presented in this study are available on request from the corresponding author. The data are not publicly available due to privacy.

**Conflicts of Interest:** The authors declare that they have no known competing financial interests or personal relationships that could have appeared to influence the work reported in this paper.

## References

1. Dissanayake, K.; Kularatna-Abeywardana, D. A review of supercapacitors: Materials, technology, challenges, and renewable energy applications. *J. Energy Storage* **2024**, *96*, 112563. [[CrossRef](#)]
2. Sharma, R.; Kumar, H.; Kumar, G.; Sharma, S.; Aneja, R.; Sharma, A.K.; Kumar, R.; Kumar, P. Progress and challenges in electrochemical energy storage devices: Fabrication, electrode material, and economic aspects. *Chem. Eng. J.* **2023**, *468*, 143706. [[CrossRef](#)]
3. Biradar, M.R.; Morajakar, P.P.; Bhosale, S.V.; Bhosale, S.V. A review on energy storage devices based on rylene imide dyes: Synthesis, applications and challenges. *Fuel* **2021**, *310*, 122487. [[CrossRef](#)]
4. Biswas, S.; Chowdhury, A. Organic Supercapacitors as the Next Generation Energy Storage Device: Emergence, Opportunity, and Challenges. *ChemPhysChem* **2023**, *24*, e202200567. [[CrossRef](#)] [[PubMed](#)]
5. Zhu, Q.; Zhao, D.; Cheng, M.; Zhou, J.; Owusu, K.A.; Mai, L.; Yu, Y. A new view of supercapacitors: Integrated supercapacitors. *Adv. Energy Mater.* **2019**, *9*, 1901081. [[CrossRef](#)]
6. Banerjee, S.; Mordini, B.; Sinha, P.; Kar, K.K. Recent advancement of supercapacitors: A current era of supercapacitor devices through the development of electrical double layer, pseudo and their hybrid supercapacitor electrodes. *J. Energy Storage* **2024**, *108*, 115075. [[CrossRef](#)]
7. Shin, S.; Gittins, J.W.; Balhatchet, C.J.; Walsh, A.; Forse, A.C. Metal–Organic Framework Supercapacitors: Challenges and Opportunities. *Adv. Funct. Mater.* **2023**, *34*, 2308497. [[CrossRef](#)]
8. Kumar, Y.A.; Yadav, A.A.; Al-Asbahi, B.A.; Kang, S.-W. Sulfur nanoparticle-decorated nickel cobalt sulfide hetero-nanostructures with enhanced energy storage for high-performance supercapacitors. *Molecules* **2022**, *27*, 7458. [[CrossRef](#)]
9. Jiang, M.; Abdullah, M.; Chen, X.; E, Y.; Tan, L.; Yan, W.; Liu, Y.; Jiang, W. Two-step synthesis of  $\text{ZnS-NiS}_2$  composite with rough nanosphere morphology for high-performance asymmetric supercapacitors. *Batteries* **2023**, *10*, 16. [[CrossRef](#)]
10. Ikhioya, I.L.; Nkele, A.C. A Novel Synthesis of Hydrothermally Prepared Europium Sulfide and Cerium Sulfide Nanomaterials Doped with Yttrium. *Arab. J. Sci. Eng.* **2023**, *49*, 1217–1225. [[CrossRef](#)]
11. Ahmed, F.B.M.; Khalafallah, D.; Zhi, M.; Hong, Z. Porous nanoframes of sulfurized NiAl layered double hydroxides and ternary bismuth cerium sulfide for supercapacitor electrodes. *Adv. Compos. Hybrid Mater.* **2022**, *5*, 2500–2514. [[CrossRef](#)]

12. Wang, L.; Zhao, T.; Chen, R.; Fang, H.; Yang, Y.; Cao, Y.; Zhang, L. Molybdenum nitride and oxide quantum dot @ nitrogen-doped graphene nanocomposite material for rechargeable lithium Ion batteries. *Batteries* **2023**, *9*, 32. [[CrossRef](#)]
13. Wu, P.; Xu, Y.; Zhan, J.; Li, Y.; Xue, H.; Pang, H. The research development of quantum dots in electrochemical energy storage. *Small* **2018**, *14*, 1801479. [[CrossRef](#)]
14. Yang, Q.; Li, Z.; Xu, B. Layered double hydroxide with interlayer quantum dots and laminate defects for high-performance supercapacitor. *Adv. Funct. Mater.* **2023**, *33*, 2300149. [[CrossRef](#)]
15. Zhang, J.; Zhang, X.; Xu, C.; Liu, Y.; Xu, J.; Miao, Z.; Yu, H.; Yan, L.; Zhang, L.; Shu, J. Dual synergistic effects assisting Cu-SeS<sub>2</sub> electrochemistry for energy storage. *Proc. Natl. Acad. Sci. USA* **2023**, *120*, e2220792120. [[CrossRef](#)]
16. Bibi, N.; Xia, Y.; Ahmed, S.; Zhu, Y.; Zhang, S.; Iqbal, A. Highly stable mesoporous CeO<sub>2</sub>/CeS<sub>2</sub> nanocomposite as electrode material with improved supercapacitor electrochemical performance. *Ceram. Int.* **2018**, *44*, 22262–22270. [[CrossRef](#)]
17. Salah, N.; Shehab, M.; El Nady, J.; Ebrahim, S.; El-Maghraby, E.; Sakr, A.-H. Polyaniline/ZnS quantum dots nanocomposite as supercapacitor electrode. *Electrochim. Acta* **2023**, *449*, 142174. [[CrossRef](#)]
18. Sahoo, S.; Satpati, A.K.; Sahoo, P.K.; Naik, P.D. Incorporation of Carbon Quantum Dots for Improvement of Supercapacitor Performance of Nickel Sulfide. *ACS Omega* **2018**, *3*, 17936–17946. [[CrossRef](#)]
19. Elnady, J.; Shaala, T.; Tork, H.M.; Soliman, M.; Ebrahim, S.; Elshaer, A.M. Acquisition of optimum co-sources of sulfur MAA capped-ZnS quantum dots conditions for photoluminescence chlorine sensor. *J. Mater. Sci. Mater. Electron.* **2021**, *32*, 16831–16844. [[CrossRef](#)]
20. Lu, C.; Tu, C.; Yang, Y.; Ma, Y.; Zhu, M. Construction of Fe<sub>3</sub>O<sub>4</sub>@Fe<sub>2</sub>P heterostructures as electrode materials for supercapacitors. *Batteries* **2023**, *9*, 326. [[CrossRef](#)]
21. Morariu, M.I.; Nicolaescu, M.; Hulka, I.; Duțeanu, N.; Orha, C.; Lăzău, C.; Bandas, C. Fabrication of Cu<sub>2</sub>O/CuO Nanowires by one-step thermal oxidation of flexible copper mesh for supercapacitor applications. *Batteries* **2024**, *10*, 246. [[CrossRef](#)]
22. Shohag, M.R.H.; Khan, M.M.R.; Saleh, M.A.; Supta, A.S.; Chowdhury, M.S.H.; Marwani, H.M.; Rahman, M.M.; Okoli, O. Easy fabrication of L-glutamic acid/ZnS composites for efficient photo-catalytic and supercapacitor performance. *RSC Adv.* **2023**, *13*, 24343–24352. [[CrossRef](#)] [[PubMed](#)]
23. Powder Diffraction File for Cerium Sulfide (CeS<sub>2</sub>); International Centre for Diffraction Data: Newtown Square, PA, USA, 2023.
24. Powder Diffraction File for Zinc Sulfide (ZnS); International Centre for Diffraction Data: Newtown Square, PA, USA, 2023.
25. Yang, X.; Xu, J.; Chen, X.; Lei, Y.; Wang, L.; Cheng, S.; Li, Y.; Lu, Y.; Zhu, Y.; Chen, N. Preparation and Characterization of Porous Carbon from Mixed Leaves for High-Performance Supercapacitors. *Chin. J. Chem.* **2021**, *39*, 353–359. [[CrossRef](#)]
26. E, Y.; Shen, X.; Chen, X.; Jiang, M.; Yan, W.; Liu, Y.; Jiang, W.; Abdullah, M. Preparation of biomass composite activated carbon based supercapacitor materials and their application in energy storage devices. *Chem. Eng. Sci.* **2023**, *282*, 119193. [[CrossRef](#)]
27. Moyseowicz, A. Scalable one-pot synthesis of bismuth sulfide nanorods as an electrode active material for energy storage applications. *J. Solid State Electrochem.* **2019**, *23*, 1191–1199. [[CrossRef](#)]
28. Tong, Y.; Dai, M.; Xing, L.; Liu, H.; Sun, W.; Wu, X. Asymmetric Hybrid Capacitor Based on NiCo<sub>2</sub>O<sub>4</sub> Nanosheets Electrode. *Acta Phys. Chim. Sin.* **2020**, *36*, 1903046. [[CrossRef](#)]
29. Yan, W.; Chen, X.; Wang, Z.; Zhao, Z.; Liu, Y.; Muhammad, A. Bi<sub>2</sub>O<sub>3</sub>/Bi<sub>2</sub>S<sub>3</sub> rod/sheet nanocomposites as battery-type materials for supercapacitors. *Chem. Eng. J.* **2024**, *504*, 158864. [[CrossRef](#)]
30. Runfa, L.; Chen, X.; Hongliang, C.; Wei, Y.; Yuanfang, Z.; Siyu, C.; Wenrui, J.; Qi, Z.; Yi, E.; Meng, J.; et al. Facile synthesis of Ni<sub>3</sub>Se<sub>4</sub>/Ni<sub>0.6</sub>Zn<sub>0.4</sub>O/ZnO nanoparticle as high-performance electrode materials for electrochemical energy storage device. *Nanotechnology* **2023**, *34*, 185401. [[CrossRef](#)]
31. Wang, Y.; Liu, Y.; Zhang, H.; Duan, X.; Ma, J.; Sun, H.; Tian, W.; Wang, S. Carbonaceous materials in structural dimensions for advanced oxidation processes. *Chem. Soc. Rev.* **2025**, *54*, 2436–2482. [[CrossRef](#)]
32. Rabanian, A.; Neghabi, M.; Zadsar, M.; Jafari, M. Theoretical studies of energy states of CdSe/ZnS/CdSe and ZnS/CdSe/ZnS quantum dots with an impurity. *Mater. Sci. Eng. B* **2021**, *274*, 115489. [[CrossRef](#)]
33. Đorđević, L.; Arcudi, F.; Cacioppo, M.; Prato, M. A multifunctional chemical toolbox to engineer carbon dots for biomedical and energy applications. *Nat. Nanotechnol.* **2022**, *17*, 112–130. [[CrossRef](#)]
34. Zhang, J.; Xie, Y.; Jiang, Q.; Guo, S.; Huang, J.; Xu, L.; Wang, Y.; Li, G. Facile synthesis of cobalt cluster-CoN<sub>x</sub> composites: Synergistic effect boosts electrochemical oxygen reduction. *J. Mater. Chem. A* **2022**, *10*, 16920–16927. [[CrossRef](#)]
35. Khan, U.A.; Iqbal, N.; Noor, T.; Ahmad, R.; Ahmad, A.; Gao, J.; Amjad, Z.; Wahab, A. Cerium based metal organic framework derived composite with reduced graphene oxide as efficient supercapacitor electrode. *J. Energy Storage* **2021**, *41*, 102999. [[CrossRef](#)]
36. Kumaresan, L.; Shanmugavelayutham, G.; Saravanan, P. Single-phase ferromagnetic iron nitride ( $\epsilon$ -Fe<sub>3</sub>N) nanoparticles synthesized by thermal plasma method for oxygen evolution and supercapacitor applications. *Appl. Phys. A* **2022**, *128*, 1073. [[CrossRef](#)]

37. Liu, S.; Chen, J.; Zhang, C.; Jin, L.; Yang, Q. Experimental study on lithium-ion cell characteristics at different discharge rates. *J. Energy Storage* **2021**, *45*, 103418. [[CrossRef](#)]
38. Zheng, W. IR compensation for electrocatalysis studies: Considerations and recommendations. *ACS Energy Lett.* **2023**, *8*, 1952–1958. [[CrossRef](#)]

**Disclaimer/Publisher’s Note:** The statements, opinions and data contained in all publications are solely those of the individual author(s) and contributor(s) and not of MDPI and/or the editor(s). MDPI and/or the editor(s) disclaim responsibility for any injury to people or property resulting from any ideas, methods, instructions or products referred to in the content.